

Nuclear volume effects in kinetic isotope fractionation: A case study of mercury oxidation by chlorine species

Chenlu Yang¹  · Yining Zhang² · Yun Liu^{1,2}

Received: 5 March 2024 / Revised: 13 March 2024 / Accepted: 26 March 2024 / Published online: 7 April 2024

© The Author(s), under exclusive licence to Science Press and Institute of Geochemistry, CAS and Springer-Verlag GmbH Germany, part of Springer Nature 2024

Abstract It is well-known that the equilibrium isotope fractionation of mercury (Hg) includes classical mass-dependent fractionations (MDFs) and nuclear volume effect (NVE) induced mass-independent fractionations (MIFs). However, the effect of the NVE on these kinetic processes is not known. The total fractionations (MDFs + NVE-induced MIFs) of several representative Hg-incorporated substances were selected and calculated with ab initio calculations in this work for both equilibrium and kinetic processes. NVE-induced MIFs were calculated with scaled contact electron densities at the nucleus through systematic evaluations of their accuracy and errors using the Gaussian09 and DIRAC19 packages (named the electron density scaling method). Additionally, the NVE-induced kinetic isotope effect (KIE) of Hg isotopes are also calculated with this method for several representative Hg oxidation reactions by chlorine species. Total KIEs for $^{202}\text{Hg}/^{198}\text{Hg}$ ranging from $-2.27\text{\textperthousand}$ to $0.96\text{\textperthousand}$ are obtained. Three anomalous ^{202}Hg -enriched KIEs ($\delta^{202}\text{Hg}/^{198}\text{Hg} = 0.83\text{\textperthousand}$, $0.94\text{\textperthousand}$, and $0.96\text{\textperthousand}$) caused by the NVE are observed, which are quite different from the classical view (i.e., light isotopes react faster than the heavy ones). The electron density scaling method we developed in this study can provide an easier way to calculate the NVE-induced KIEs for heavy isotopes and serve to better understand the fractionation mechanisms of mercury isotope systems.

✉ Yun Liu
liuyun@vip.gyig.ac.cn

¹ Research Center for Planetary Science, College of Earth and Planetary Sciences, Chengdu University of Technology, Chengdu 610059, China

² State Key Laboratory of Ore Deposit Geochemistry, Institute of Geochemistry, Chinese Academy of Sciences, Guiyang 550081, China

Keywords Nuclear volume effect · Kinetic fractionation · Hg isotopes · Ab initio calculations

1 Introduction

As an important diagenetic and metallogenic element widely distributed and one of the most toxic heavy metal pollutants, mercury is widely used to trace biogeochemical reaction processes, global mercury cycle processes, and mercury pollution (Xu et al. 2021). Hundreds of works have focused on the characteristics of mercury isotope compositions, including definitions, variations in natural samples, and fractionation mechanisms (Blum et al. 2014; Blum and Johnson 2017). Due to the diverse chemical behaviors of mercury in different redox states, fractionations of Hg isotopes have been widely used as a redox tracer (Blum 2011). Different chemical mechanisms lead to the fractionation of mercury isotopes, including biological and abiotic MDFs, and MIFs caused by the magnetic isotope effect (MIE) and NVE (Bergquist and Blum 2007, 2009; Estrade et al. 2009). They can be used to trace the boiling of fluid during the process of mineralization (Smith et al. 2005; Fu et al. 2020; Liu et al. 2021), the source of ore-forming materials (Xu et al. 2018; Zhu et al. 2020), etc.

Mercury is a transition metal with strong sulfur (S) and copper (Cu) affinity. Mercury exists in three main oxidation states: Hg (0) (elemental mercury), Hg (I) (mercurous mercury) and Hg (II) (mercuric mercury). The most common oxidation state in natural solid substances is mercury (II), which usually forms sulfide, chloride, selenide and telluride (Blum and Johnson 2017). There are seven stable isotopes of mercury in nature (^{196}Hg , ^{198}Hg , ^{199}Hg , ^{200}Hg , ^{201}Hg , ^{202}Hg and ^{204}Hg), and their abundances are 0.15%, 10.04%, 16.94%, 23.14%, 13.18% and 6.82% respectively

according to Bergquist and Blum (2007). For high-precision mercury isotope measurements, these MIFs of Hg isotopes are defined as the deviations between the measured mercury isotope values and the calculated ones based on the theoretical mass fractionation law and are expressed as follows (Li et al. 2005; Bergquist and Blum 2007):

$$\Delta^{199}\text{Hg} = \delta^{199}\text{Hg} - (\delta^{202}\text{Hg} \times 0.2520)$$

$$\Delta^{200}\text{Hg} = \delta^{200}\text{Hg} - (\delta^{202}\text{Hg} \times 0.5024)$$

$$\Delta^{201}\text{Hg} = \delta^{201}\text{Hg} - (\delta^{202}\text{Hg} \times 0.7520)$$

$$\Delta^{204}\text{Hg} = \delta^{204}\text{Hg} - (\delta^{202}\text{Hg} \times 1.4930)$$

where $\delta^X\text{Hg}(\%)$ represents the composition of mercury isotopes, that is, the deviation of the sample from the standard material (e.g., NIST SRM3133). Mercury is one of the few elements with both significant MDFs and MIFs. Two types of MIFs have been observed for mercury isotopes: odd-numbered ($\Delta^{199}\text{Hg}$ and $\Delta^{201}\text{Hg}$) in photochemical reactions and even-numbered MIFs ($\Delta^{200}\text{Hg}$ and $\Delta^{204}\text{Hg}$) associated with the photoredox of atmospheric tropopause mercury (Bergquist and Blum 2007; Chen et al. 2012; Yin et al. 2014; Sun et al. 2019). These specific physicochemical and biological processes make it an advantageous tool to study the mercury cycle. The NVE and MIE are believed to be the two main causes of odd-numbered mercury isotope MIFs (Dzurko et al. 2009; Li et al. 2016; Lin et al. 2020). Nowadays, many experimental studies have confirmed the effect of NVE during volatilization, reduction, and adsorption of liquid mercury. For example, the ratio or slope of $\Delta^{199}\text{Hg}/\Delta^{201}\text{Hg}$ caused by NVE is approximately 1.5–1.6 (Sial et al. 2013; Yang and Liu 2015; Sun et al. 2016; Thibodeau et al. 2016).

To our knowledge, nearly all theoretical works have focused on the NVE of equilibrium mercury isotope fractionation (e.g., Schauble 2007; Yang and Liu 2015, 2016). However, how the NVE performs for these kinetic isotope effects (KIEs) remains to be explored. Theoretically, significant NVE-induced kinetic mercury isotope fractionations can be expected. Therefore, based on previous works, we first calculated the equilibrium isotope mass fractionation of mercury-containing species through ab initio calculations via two different methods. Several representative Hg-related substances, Hg^0 , Hg^+ , Hg^{2+} , HgCl_2 , HgBr_2 , $\text{Hg}(\text{CH}_3)_2$, $\text{Hg}(\text{CH}_3)\text{Cl}$, $[\text{Hg}(\text{H}_2\text{O})_6]^{2+}$, $\text{Hg}(\text{OH})_2$ and $[\text{HgCl}_4]^{2-}$ were selected. Both equilibrium MDFs and NVE-induced MIFs were calculated. Furthermore, since experiments have shown that mercury chlorine species are the main products of coal combustion, the study of the mechanism and the mercuric chloride species are conducive to controlling the emission of mercury from air pollutants. The

kinetic isotope fractionations of mercury oxidation by chlorine species also calculated by taking 6 mercury oxidation reactions with chlorine species from Li et al. (2003) as follows:



Reactions 4 and 5 belong to the same reaction because this reaction goes through two steps: (1) HgO reacts with HCl through transition state TS to form intermediate M; (2) Intermediate M decomposes into the final products through transition state TS'. Two different Hg atoms in Reaction 6 were calculated separately, and the results are approximated as their averages. Finally, the total KIEs (MDFs+NVE-induced MIFs) of these 6 reactions were calculated.

2 Methods

2.1 Isotope fractionations

Considering whether an isotopic exchange reaction reaches equilibrium or not, isotope fractionations can be simply divided into equilibrium isotope fractionations and kinetic isotope fractionations.

2.1.1 Equilibrium isotope mass-dependent fractionation

For an isotope exchange reaction, Urey (1947) and Bigeleisen and Mayer (1947) proposed the classical isotope equilibrium fractionation theory by adopting the ideal gas hypothesis, Born Oppenheimer Approximation (BOA), rigid rotator and harmonic oscillator approximations and the Teller-Redlich production rule (Redlich 1935). For a reaction involving only one substitutable X atom with X^* denoting its heavy isotope, the equilibrium isotopic fractionation factor α_{AX-BX} between AX and BX molecules can be expressed as:

$$\alpha_{AX-BX} = \frac{\text{RPFR}(AX^*/AX)}{\text{RPFR}(BX^*/BX)} \quad (7)$$

RPFR is called the reduced partition function ratio of an isotopologue pair and is expressed as:

$$\text{RPFR}(\text{AX}^*/\text{AX}) = \frac{\frac{q_{\text{AX}}^*}{q_{\text{AX}}}}{\frac{\sigma}{\sigma^*} \left(\frac{m^*}{m} \right)^{\frac{3}{2}}} = \prod_i \frac{u_i^*}{u_i} \frac{e^{-u_i^*/2}}{e^{-u_i/2}} \frac{1 - e^{-u_i}}{1 - e^{-u_i^*}} \quad (8)$$

where σ is the rotational symmetry number, q is the partition function, and m and m^* are the masses of X and X^* , respectively. $u = \frac{hv}{k_B T} = \frac{hc\omega}{k_B T}$ where h is the Planck constant, k_B is the Boltzmann constant and T is the temperature in kelvin. v and ω are the harmonic vibrational frequencies in Hz and wavenumber cm^{-1} , respectively.

2.1.2 Kinetic isotope fractionation

The classical theory of kinetic isotope fractionation for an elementary reaction ($A \rightarrow B$) was proposed by Bigeleisen and Wolfsberg (1958) through combining the canonical transition state theory (CTST) (Eyring 1935) with the classical equilibrium isotope fractionation theory (Urey 1947; Bigeleisen and Mayer 1947). The kinetic isotope fractionation factor (α_{KIE} , heavy over light will be used in this study) can be expressed by the ratio of two RPFRs between the transition state (A^\ddagger) and the reactant (A) as:

$$\alpha_{\text{KIE}} = \frac{v^{\ddagger*}}{v^\ddagger} \frac{\text{RPFR}(A^\ddagger)}{\text{RPFR}(A)} \quad (9)$$

where v^\ddagger denotes the imaginary vibrational mode along the reaction path at the saddle point. By excluding this imaginary mode, the RPFR value of the transition state is defined as:

$$\text{RPFR}(A^\ddagger) = \prod_{i=1}^{3N-7} \frac{u_i^*}{u_i} \frac{e^{-u_i^*/2}}{e^{-u_i/2}} \frac{1 - e^{-u_i}}{1 - e^{-u_i^*}} \quad (10)$$

where $3N - 7$ means that one degree of freedom for the imaginary vibration mode is excluded for a non-linear transition state (for a linear transition state, $3N - 6$ degrees of freedom will be used). For most kinetic processes $\alpha_{\text{KIE}} < 1$, the reaction rate of light isotopes is faster than that of heavy isotopes.

2.2 Nuclear volume effect (NVE)

Because the MDFs are proportional to the relative mass difference between two isotopes, they will be rather small for heavy isotope systems with large atomic numbers. The nuclear volume effect (NVE) is actually a simplified nuclear field shift effect (NFSE) (King 1984; Fujii et al. 2009). Previously, researchers such as Stacey (1966), Aufmuth et al. (1987) first proposed the concept of nuclear field shift effect, i.e., an electronic energy shift between

two isotopes due to a slight change in the nuclear charge distribution-induced variations in static electric fields. When the atomic number Z becomes large (generally larger than 40), the NFSE becomes significant and must be carefully checked for heavy isotope systems (e.g., Schable 2007, 2013; Yang and Liu 2015, 2016; Fang and Liu 2019). The magnitude of the NFSE depends on the electron density at the nucleus and the charge, shape, and size of the nucleus (Bigeleisen 1996). In this study, the commonly used Gaussian model (spherical) for nuclear charge distribution was adopted to estimate NFSE, so only the effect of charge size of the nucleus, i.e., the volume, which is therefore called the nuclear volume effect was considered (Schauble 2007, 2013; Yang and Liu 2015, 2016). Currently, two methods have been proposed for calculating the NVE through ab initio calculations. The first one is to calculate the electronic energy difference of the two isotopes (which can be named as the energy method), whose fractionation factor, $K_{\text{fs}}(\text{AY} - \text{AX})$, can be expressed as (e.g., Schable 2013; Yang and Liu 2015, 2016):

$$\ln K_{\text{fs}} = \frac{1}{k_B T} \{ [E^0(A'X) - E^0(AX)] - [E^0(A'Y) - E^0(AY)] \} \quad (11)$$

where AX and AY represent two different substances containing the same element A, respectively. A and A' represent the light and heavy isotopes of element A, respectively. E^0 is the calculated electronic energy.

The second one estimates the NVE by adopting the electron density at the nucleus (named the density method) as in (Almoukhhalati et al. 2016; Fang and Liu 2019):

$$\ln K_{\text{fs}} = \frac{1}{k_B T} \frac{Z_A e^2}{6\epsilon_0} [\bar{\rho}_e^A(AX) - \bar{\rho}_e^A(AY)] \delta r_{AA'}^2 \quad (12)$$

where Z_A is the atomic number of element A, e is an elementary charge ($1.60217733 \times 10^{-19} \text{ C}$), ϵ_0 is the permittivity of vacuum ($8.854187817 \times 10^{-12} \text{ F/m}$), and $\delta(r^2)_{AA'}$ represents the mean square deviation of the nuclear charge radius between light and heavy isotopes with $\delta(r^2)_{AA'} = \langle r^2 \rangle_{A'} - \langle r^2 \rangle_A$ (Angeli 2004; Angeli and Marinova 2013). For Hg isotopes, the radius data of Angeli (2004) are used here for comparison with the data of Schable (2007). Thus, the nuclear charge radius data of Angeli (2004) are used in equilibrium isotope fractionation. $\bar{\rho}_e^A$ is called the effective electron density at the nucleus of A in the target substance. Since $\bar{\rho}_e^A$ is actually the electron density within a certain radius of the nuclear center, it can also be approximated as the electron density at the origin $\mathbf{r} = 0$, that is, the contact electron density ($|\Psi(0)|^2$). However, such an approximation will generally cause a systematic error of about 10% (Almoukhhalati et al. 2016).

2.3 Ab-initio calculations

First, to evaluate the precision and accuracy of our ab initio calculations, several representative Hg-incorporated species, Hg^0 , Hg^+ , Hg^{2+} , HgCl_2 , HgBr_2 , $\text{Hg}(\text{CH}_3)_2$, $\text{Hg}(\text{CH}_3)\text{Cl}$, $[\text{Hg}(\text{H}_2\text{O})_6]^{2+}$, $\text{Hg}(\text{OH})_2$ and $[\text{HgCl}_4]^{2-}$ from Schauble (2007) were chosen for the test and validation calculations. For equilibrium MDFs (denoted as $1000\ln\beta^{\text{MD}}$), the classical theory and method proposed by Bigeleisen and Mayer (1947) and Urey (1947) are used with these harmonic vibrational frequencies obtained by the Gaussian09 D.01 package (Frisch et al. 2009). For NVEs, we followed the methods and procedures used by Schauble (2007) and Yang and Liu (2015).

The equilibrium geometry and harmonic vibrational frequencies are optimized and calculated by the Gaussian09 D.01 package (Frisch et al. 2009) using density functional theory (DFT) with the B3LYP exchange–correlation functional (Becke 1993). For Hg, the double-zeta cc-pVDZ-PP with a relativistic effective core potential (ECP) (Peterson and Puzzarini 2005) was adopted. For these light elements (H, C, O, Cl and Br), the double-zeta correlation-consistent basis set of cc-pVDZ was used (Dunning 1989; Wilson et al. 1999). We choose DIRAC19 software (Gomes et al. 2019) to perform all-electron relativistic calculations for NVE using effective electron density methods (Almoukhalaati et al. 2016). The relativistic electronic structure is calculated by four-component all-electron Dirac–Hartree–Fock (DHF) and B3LYP methods. The optimized geometries with Gaussian09 D.01 were used for DIRAC calculations. For these DIRAC calculations, the uncontracted Dyall's double-zeta all-electron basis set dyall.ae2z (Dyall 2023) was adopted for Hg atoms, and the uncontracted cc-pVDZ basis set was used for these light elements (H, C, O, Cl, and Br). In particular, nuclear charge radius data from Angeli (2004) are used here for comparison with previous works (e.g., Schauble 2007). All the nuclear volume effect (NVE) fractionation factors (denoted as $1000\ln\beta^{\text{NV}}$) and the total fractionation factors (denoted as $1000\ln\beta$) were compared with the results of Schauble (2007) and Yang and Liu (2015) to validate the accuracy of the calculations in this study (Table 1).

Second, we calculated the contact densities by Gaussian09 D.01 and Multiwfns 3.8(dev) (Lu and Chen 2012) at the B3LYP level with 4 different settings (two different all-electron basis sets for Hg atoms, SARC-DKH2 (Pantazis et al. 2008) and x2c-QZVPPall (Franzke et al. 2020) with second-order Douglas–Kroll–Hess scalar relativistic corrections (DKH2, Barysz and Sadlej 2001) or not: SARC-DKH2, SARC-DKH2 + DKH2, x2c-QZVPPall and x2c-QZVPPall + DKH2. Because the contact electron density calculated by Gaussian09 D.01 is relatively rough compared to these effective densities calculated by DIRAC and these precise and accurate DIRAC calculations are always too

expensive to be applied for medium and large systems, we fitted the results of Gaussian09 D.01 with these of DIRAC19 with DHF and B3LYP methods, respectively, to obtain a scaling factor for these Gaussian09 results to reproduce “accurate” relativistic DIRAC effective densities with rough contact density calculated by Gaussian09 D.01 with acceptable and controllable errors.

Finally, a transition state search and corresponding frequency analysis for the 6 reactions above were performed with Gaussian09 D.01. The B2-PLYP double-hybrid DFT functional (Grimme 2006) was adopted with the DFT-D3 dispersion correction (Grimme et al. 2010). The triple-zeta basis set def2-TZVP with ECP (Weigend and Ahlrichs 2005) was used for Hg, and cc-pVDZ was used for light elements (H, C, O, Cl and Br). All 6 transition states (TSs) were successfully searched, and it was confirmed that there was only one imaginary vibrational mode at the saddle point along the reaction path for each transition state. The corresponding contact densities for all the Hg-incorporated species of the reactants and the transitions of all 6 reactions were calculated by the combination of Gaussian09 D.01 with Multiwfns 3.8 (dev) using the same 4 different settings: SARC-DKH2; SARC-DKH2 + DKH2; x2c-QZVPPall; and x2c-QZVPPall + DKH2. Then, these contact densities are scaled to reproduce the corresponding pseudo-DIRAC results. Meanwhile, the effective electron density data for Hg atoms were also calculated with DIRAC19 with both DHF and B3LYP methods using the same basis sets above (Hg: dyall.ae2z; Light elements: cc-pVDZ) to evaluate the accuracy of those scaled results. Due to the improved calculation method compared with the data of Angeli (2004), the deviation between the calculated data and the experimental results is reduced from Angeli and Marinova (2013). Finally, these corresponding total KIEs (also denoted as $1000\ln\beta^{\text{MD}}$, $1000\ln\beta^{\text{NV}}$ and $1000\ln\beta$ values) for these 6 reactions were calculated with the latest and more accurate nuclear charge radius data from Angeli and Marinova (2013).

3 Results

3.1 Equilibrium isotope mass dependence and nuclear volume fractionations

Table 1 shows our calculated equilibrium fractionation factors $1000\ln\beta_{202-198}^{\text{MD}}$ (MDFs), $1000\ln\beta_{202-198}^{\text{NV}}$ (NVE-induced MIFs) and $1000\ln\beta_{202-198}$ (total fractionations) of Hg^0 , Hg^+ , Hg^{2+} , HgCl_2 , HgBr_2 , $\text{Hg}(\text{CH}_3)_2$, $\text{Hg}(\text{CH}_3)\text{Cl}$, $[\text{Hg}(\text{H}_2\text{O})_6]^{2+}$, $\text{Hg}(\text{OH})_2$ and $[\text{HgCl}_4]^{2-}$ and their comparison with those of Schauble (2007) (DIRAC04) and Yang and Liu (2015) (DIRAC13.1) from 273 to 573 K. The nuclear charge radius data of Angeli (2004) were used for consistency when compared with those of Schauble (2007). Our results are in good

Table 1 Calculated stable isotope fractionation factors for Hg-bearing species relative to Hg^0 (%), including conventional mass-dependent effect (MD) and $(1000\ln\beta_{202-198}^{\text{MD}})$, nuclear volume effect (NVE) ($1000\ln\beta_{202-198}^{\text{NV}}$) and total fractionations ($1000\ln\beta_{202-198}$)

Species	This study				Schauble (2007) ^a				Yang and Liu (2015) ^b			
	273 K	298 K	373 K	573 K	273 K	298 K	373 K	573 K	273 K	298 K	373 K	573 K
MD fractionation factors ($1000\ln\beta_{202-198}^{\text{MD}}$)												
Hg^0	0	0	0	0	0	0	0	0	0	0	0	0
Hg^+	0	0	0	0	0	0	0	0	0	0	0	0
Hg^{2+}	0	0	0	0	0	0	0	0	0	0	0	0
HgCl_2	0.97	0.82	0.53	0.23	1.08	0.92 ± 0.1	0.6	0.26	1.00	0.84	0.55	0.24
HgBr_2	0.84	0.71	0.46	0.20	0.95	0.80 ± 0.1	0.51	0.22	0.88	0.74	0.48	0.21
$\text{Hg}(\text{CH}_3)_2$	1.09	0.93	0.62	0.27	1.14	0.97 ± 0.1	0.65	0.29	1.13	0.97	0.64	0.28
$\text{Hg}(\text{CH}_3)\text{Cl}$	0.99	0.84	0.55	0.24	1.04	0.89 ± 0.1	0.58	0.25	1.02	0.87	0.57	0.25
$[\text{Hg}(\text{H}_2\text{O})_6]^{2+}$	1.08	0.92	0.59	0.26	1.13	0.96 ± 0.4	0.62	0.27	0.71	0.60	0.39	0.17
$\text{Hg}(\text{OH})_2$	1.42	1.21	0.81	0.36					1.54	1.32	0.88	0.39
$[\text{HgCl}_4]^{2-}$	0.48	0.40	0.26	0.11	0.67	$0.56 + 0.7 / -0.1$	0.36	0.15	0.49	0.41	0.26	0.11
NVE fractionation factors ($1000\ln\beta_{202-198}^{\text{NV}}$)												
Hg^0	0	0	0	0	0	0	0	0	0	0	0	0
Hg^+	1.38	1.26	1.01	0.66								
Hg^{2+}	3.47	3.18	2.54	1.65	3.47	3.17 ± 0.6	2.54	1.65	3.94	3.61	2.89	1.88
HgCl_2	1.39	1.27	1.02	0.66	1.39	1.27 ± 0.3	1.02	0.66	1.58	1.45	1.16	0.75
HgBr_2	1.32	1.21	0.97	0.63	1.34	1.23 ± 0.2	0.98	0.64	1.53	1.4	1.12	0.73
$\text{Hg}(\text{CH}_3)_2$	0.62	0.57	0.45	0.29	0.62	0.57 ± 0.1	0.45	0.3	0.71	0.65	0.52	0.34
$\text{Hg}(\text{CH}_3)\text{Cl}$	0.86	0.79	0.63	0.41	0.88	0.80 ± 0.2	0.64	0.42	0.99	0.91	0.73	0.47
$[\text{Hg}(\text{H}_2\text{O})_6]^{2+}$	2.97	2.72	2.18	1.42	3.01	2.75 ± 0.6	2.2	1.43	3.45	3.16	2.52	1.64
$\text{Hg}(\text{OH})_2$	1.15	1.05	0.84	0.55					1.22	1.12	0.9	0.58
$[\text{HgCl}_4]^{2-}$	2.42	2.21	1.77	1.15	2.42	2.22 ± 0.4	1.77	1.16	2.76	2.53	2.02	1.31
Total fractionations ($1000\ln\beta_{202-198}$)												
Hg^0	0	0	0	0	0	0	0	0	0	0	0	0
Hg^+	1.38	1.26	1.01	0.66								
Hg^{2+}	3.47	3.18	2.54	1.65	3.47	3.17 ± 0.6	2.54	1.65	3.94	3.61	2.89	1.88
HgCl_2	2.36	2.09	1.55	0.89	2.47	2.19 ± 0.3	1.62	0.92	2.58	2.29	1.71	0.99
HgBr_2	2.16	1.92	1.42	0.82	2.29	2.03 ± 0.2	1.49	0.86	2.41	2.14	1.6	0.94
$\text{Hg}(\text{CH}_3)_2$	1.71	1.50	1.07	0.57	1.76	1.54 ± 0.1	1.1	0.59	1.84	1.62	1.16	0.62
$\text{Hg}(\text{CH}_3)\text{Cl}$	1.85	1.63	1.18	0.65	1.92	1.69 ± 0.2	1.22	0.67	2.01	1.78	1.3	0.72
$[\text{Hg}(\text{H}_2\text{O})_6]^{2+}$	4.05	3.64	2.77	1.67	4.14	3.17 ± 0.7	2.82	1.7	4.16	3.76	2.91	1.81
$\text{Hg}(\text{OH})_2$	2.56	2.26	1.65	0.91					2.76	2.44	1.78	0.97
$[\text{HgCl}_4]^{2-}$	2.89	2.61	2.02	1.26	3.09	$2.78 + 0.8 / 0.4$	2.13	1.31	3.25	2.94	2.28	1.42

^aCalculated by DIRAC04 from Schäuble (2007)^bCalculated by DIRAC13.1 from Yang and Liu (2015)

agreement with the data from Schäuble (2007). The maximum error of MDFs exists between our results (0.48 %) and those of Schäuble (2007) (0.67 %) for $[\text{HgCl}_4]^{2-}$ at 273 K. For NVE-induced MIFs, a maximum error of 0.04 % was observed for $[\text{Hg}(\text{H}_2\text{O})_6]^{2+}$ at 273 K.

Compared with the data of Yang and Liu (2015), our results for $1000\ln\beta_{202-198}^{\text{MD}}$ are in good agreement. However, systematic overestimations of $1000\ln\beta_{202-198}^{\text{NV}}$ exist. We believe that this discrepancy can be attributed to the difference in the nuclear charge radius ($\langle r^2 \rangle_{198,202}$) between ours and that of Yang and Liu (2015). In their study, the data of

Fricke and Heilig (2004) were adopted through DIRAC13.1, which is 13.7% larger than the one we used in this study. With simple scaling (1/1.137) of their results, the maximum error of $1000\ln\beta_{202-198}^{\text{NV}}$ significantly decreased to only 0.09 %.

3.2 Correlations and linear fittings between the contact and effective densities

Correlations and linear fitting results between these contact density differences relative to Hg^0 ($\Delta|\Psi(0)|^2$)

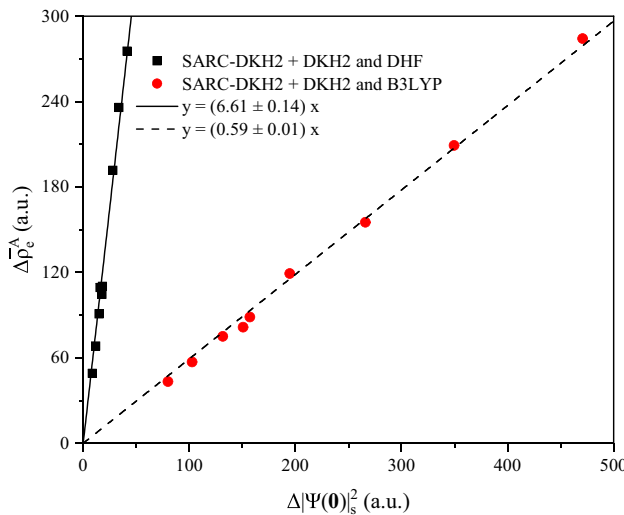


Fig. 1 Density difference fitting of the SARC-DKH2 basis set with the DKH2 relativistic effects with the B3LYP and DHF methods for mercury-related substances

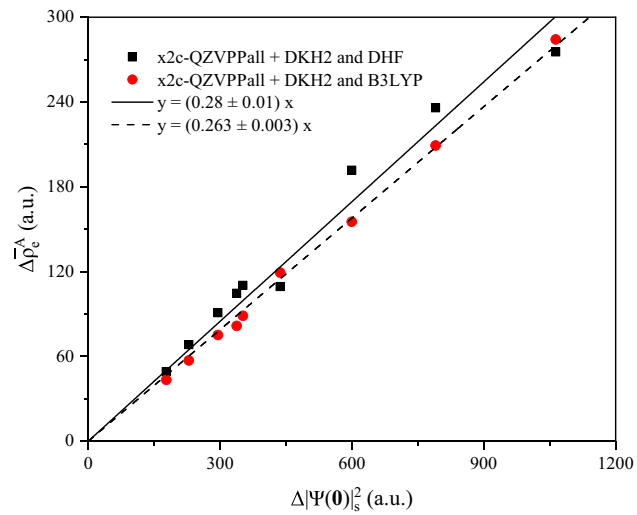


Fig. 3 Density difference fitting of the x2c-QZVPPall basis set with the DKH2 relativistic effects with the B3LYP and DHF methods for mercury-related substances

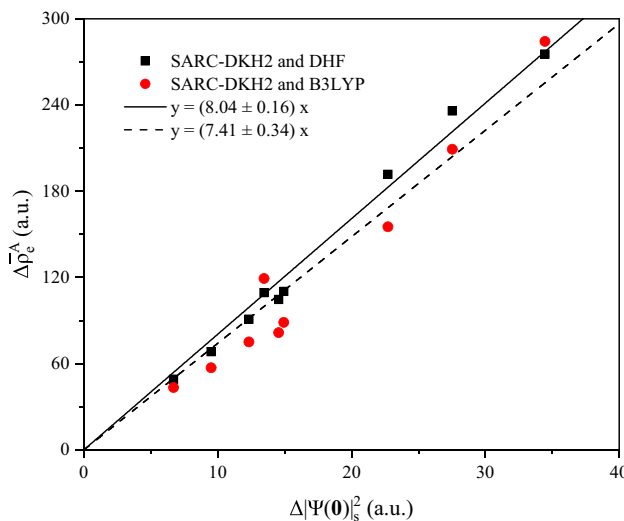


Fig. 2 Density difference fitting of the SARC-DKH2 basis set without the DKH2 relativistic effects with the B3LYP and DHF methods for mercury-related substances

calculated with Gaussian09 D.01 with Multiwfn 3.8(dev) (4 sets at the B3LYP level: SARC-DKH2 + DKH2; SARC-DKH2; x2c-QZVPPall + DKH2; x2c-QZVPPall) and the corresponding effective density differences ($\Delta\bar{\rho}_e^A$) calculated with DIRAC19 (2 sets at the DHF and B3LYP levels) are plotted in Figs. 1, 2, 3, 4. Four sets of linear fitted scale factors/slopes (8 in total) are obtained:

SARC-DKH2 + DKH2 (Fig. 1):

DIRAC-DHF: 6.61 ± 0.14 ;

DIRAC-B3LYP: 0.59 ± 0.01 .

SARC-DKH2 (Fig. 2):

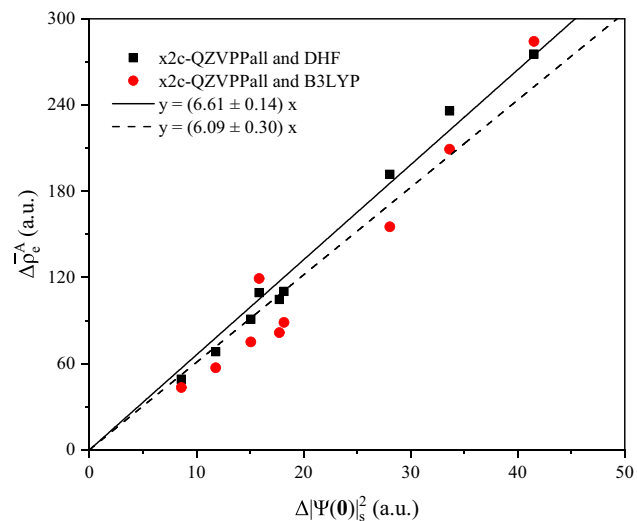


Fig. 4 Density difference fitting of the x2c-QZVPPall basis set without the DKH2 relativistic effects with the B3LYP and DHF methods for mercury-related substances

DIRAC-DHF: 8.04 ± 0.16 ;

DIRAC-B3LYP: 7.41 ± 0.34 .

x2c-QZVPPall + DKH2 (Fig. 3):

DIRAC-DHF: 0.28 ± 0.01 ;

DIRAC-B3LYP: 0.263 ± 0.003 .

x2c-QZVPPall (Fig. 4):

DIRAC-DHF: 6.61 ± 0.14 ;

DIRAC-B3LYP: 6.09 ± 0.30 .

All 4 sets of data with 8 fittings in total show well linearity with relatively small standard errors for slopes, indicating that good linear correlations between $\Delta|\Psi(0)|^2$ and

$\Delta\bar{\rho}_e^A$ can be expected and applied for other isotope systems and processes. Additionally, we noticed that these $\Delta|\Psi(0)|^2$ results without DKH2 corrections show significant underestimations when compared to the corresponding $\Delta\bar{\rho}_e^A$ values, which may be directly related to the neglection of relativistic effects.

The fitting errors of the density difference results among these four sets of linear fitting results are also obtained (root mean standard errors):

SARC-DKH2 + DKH2:

DIRAC-DHF: 13.8;

DIRAC-B3LYP: 11.6

SARC-DKH2:

DIRAC-DHF: 8.9;

DIRAC-B3LYP: 18.5

x2c-QZVPPall + DKH2:

DIRAC-DHF: 14.0;

DIRAC-B3LYP: 4.0

x2c-QZVPPall:

DIRAC-DHF: 14.5.

DIRAC-B3LYP: 19.9

The combination of x2c-QZVPPall + DKH2 and DIRAC-B3LYP had the smallest fitting errors.

3.3 Kinetic isotope mass dependent and nuclear volume fractionations of Hg

For all 6 reactions introduced above, these calculated activation energies (E_a in kJ/mol) at 298.15 K and the corresponding rate constants are summarized in Table 2. The activation energy was calculated by taking the Gibbs free energy (electronic energy + thermal correction) difference between the transition state and reactant with Gaussian09 D.01 at the B2-PLYP level with def2-TZVP for Hg and cc-pVDZ for light elements (H, C, O, Cl and Br). The results show that Reaction 5 has the fastest reaction rate and Reaction 2 has the slowest reaction rate. The calculated activation energy of Reaction (5) is negative different from others. Due to the presence of an intermediate state and two transition states in the process of reactants generating products through

Table 2 Activation energy E_a (kJ/mol) and reaction rate constant k (s^{-1}) of Reactions 1, 2, 3, 4, 5, 6 at 298.15 K

Reaction	E_a (kJ/mol)	$k(s^{-1})$
$Hg + HOCl \rightarrow HgCl + OH$	172.06	4.54×10^{-18}
$Hg + HCl \rightarrow HgCl + H$	434.27	1.30×10^{-63}
$HgCl + HCl \rightarrow HgCl_2 + H$	155.23	1.63×10^{-14}
$HgO + HCl \rightarrow M$	13.10	7.80×10^9
$M \rightarrow HgCl + OH$	-3.44	1.65×10^{13}
$Hg + HgCl_2 \rightarrow Hg_2Cl_2$	161.58	1.53×10^{-16}

Reactions 5 and 6. In order to facilitate readers' understanding, M is used uniformly. Therefore, it is normal for M in Reaction (5) to be used only as an intermediate in the transition state search process to calculate a negative activation energy value. The negative energy difference calculated by Li et al. (2003) also proves this point.

All the $\Delta|\Psi(0)|^2$ values calculated by Gaussian09 D.01 and Multiwfn 3.8(dev) at the B3LYP level with 4 different settings, the corresponding scaled values (denoted as $\Delta|\Psi(0)|_s^2$) using fitted scale factors/slopes in Sect. 3.2, and the $\Delta\bar{\rho}_e^A$ values calculated by DIRAC19 at both the DHF and B3LYP levels for the $^{202}\text{Hg}/^{198}\text{Hg}$ of Reactions 1, 2, 3, 4, 5, 6 are summarized in Table 3. Additionally, the corresponding $1000\ln\beta_{202-198}^{\text{NV}}$ at 273.15 K are also calculated and summarized in Table 4.

Furthermore, $1000\ln\beta_{202-198}^{\text{NV}}$ at 273.15 K calculated by $\Delta|\Psi(0)|_s^2$ (4 sets and 8 groups in total for DHF and B3LYP) and $\Delta\bar{\rho}_e^A$ (2 groups of DHF and B3LYP) are plotted and compared in Figs. 5 and 6. Generally, a better linear correlation can be observed for these results calculated at the B3LYP level (Fig. 6). We also noticed significant deviations for these data calculated at the Hartree–Fock level, especially for Reaction 5 in Fig. 5.

4 Discussion

4.1 On accuracy of NVE calculations

For the Hg-incorporate species Hg^0 , Hg^+ , Hg^{2+} , $HgCl_2$, $HgBr_2$, $Hg(CH_3)_2$, $Hg(CH_3)Cl$, $[Hg(H_2O)_6]^{2+}$, $Hg(OH)_2$ and $[HgCl_4]^{2-}$, excellent agreement between our results and those of Schable (2007) and Yang and Liu (2015) (scaled for differences in nuclear charge radius data) was obtained.

To further evaluate the accuracy of these fittings, a simple statistical analysis was performed on the $\Delta|\Psi(0)|_s^2$ and $\Delta\bar{\rho}_e^A$ values of Reactions 1, 2, 3, 4, 5, 6 and the results are summarized in Table 3. We compared our two sets of results calculated with DIRAC19 (effective density: DHF and B3LYP) with four scaled sets of results calculated by Gaussian09 D.01 + Multiwfn 3.8(dev) results (B3LYP: SARC-DKH2 + DKH2; SARC-DKH2; x2c-QZVPPall + DKH2; x2c-QZVPPall) using the slopes previously obtained in Sect. 3.1. The statistical results for this comparison are summarized in Table 5. The results show that the maximum standard deviation and average absolute error of DHF are 51.97 a.u. and 51.67 a.u. respectively, while the maximum standard deviation and average absolute error of B3LYP are 18.58 a.u. and 14.48 a.u. respectively. Therefore, at least for the 6 reactions studied in this work, the scaled contact density calculated by Gaussian09 D.01 and Multiwfn 3.8(dev) at the B3LYP level exhibited

Table 3 Calculated scaled contact density ($\Delta|\Psi(0)|_s^2$) and effective density differences ($\Delta\bar{\rho}_e^A$) for Reactions 1, 2, 3, 4, 5, 6 for $^{202}\text{Hg}/^{198}\text{Hg}$

DIRAC-DHF	$\Delta \Psi(0) _s^2$ (a.u.)				$\Delta\bar{\rho}_e^A$ (a.u.)
	SARC-DKH2 + DKH2	SARC-DKH2	x2c-QZVP-Pall + DKH2	x2c-QZVPPall	
$\text{Hg} + \text{HOCl} \rightarrow \text{HgCl} + \text{OH}$	-54.3	-76.9	-54.6	-71.0	-65.6
$\text{Hg} + \text{HCl} \rightarrow \text{HgCl} + \text{H}$	-56.1	-82.4	-56.3	-75.7	-65.3
$\text{HgCl} + \text{HCl} \rightarrow \text{HgCl}_2 + \text{H}$	-33.3	-19.9	-24.3	-19.1	-16.7
$\text{HgO} + \text{HCl} \rightarrow \text{M}$	-3.3	-4.5	-3.4	-4.6	-6.4
$\text{M} \rightarrow \text{HgCl} + \text{OH}$	-33.0	-45.8	-34.0	-43.0	-90.6
$\text{Hg} + \text{HgCl}_2 \rightarrow \text{Hg}_2\text{Cl}_2$ (Hg1)	-67.4	-64.7	-67.3	-63.0	-72.0
$\text{Hg} + \text{HgCl}_2 \rightarrow \text{Hg}_2\text{Cl}_2$ (Hg2)	0.1	10.0	-0.3	7.5	-1.0
DIRAC-B3LYP					
$\text{Hg} + \text{HOCl} \rightarrow \text{HgCl} + \text{OH}$	-50.6	-70.9	-50.9	-70.5	-51.4
$\text{Hg} + \text{HCl} \rightarrow \text{HgCl} + \text{H}$	-52.2	-76.0	-52.4	-75.2	-49.5
$\text{HgCl} + \text{HCl} \rightarrow \text{HgCl}_2 + \text{H}$	-31.0	-18.4	-22.7	-19.0	-12.6
$\text{HgO} + \text{HCl} \rightarrow \text{M}$	-3.0	-4.2	-3.1	-4.6	-4.1
$\text{M} \rightarrow \text{HgCl} + \text{OH}$	-30.7	-42.2	-31.7	-42.8	-31.4
$\text{Hg} + \text{HgCl}_2 \rightarrow \text{Hg}_2\text{Cl}_2$ (Hg1)	-62.8	-59.7	-62.7	-62.6	-58.1
$\text{Hg} + \text{HgCl}_2 \rightarrow \text{Hg}_2\text{Cl}_2$ (Hg2)	0.0	9.2	-0.3	7.5	2.6

Table 4 Calculated nuclear volume effect ($1000\ln\beta_{202-198}^{\text{NV}}$) fractionation factors at 273.15 K for Reactions 1, 2, 3, 4, 5, 6

Combination	SARC-DKH2 + DKH2	SARC-DKH2	x2c-QZVP-Pall + DKH2	x2c-QZVPPall
DIRAC-DHF	$1000\ln\beta_{202-198}^{\text{NV}}$			
$\text{Hg} + \text{HOCl} \rightarrow \text{HgCl} + \text{OH}$	0.74	1.05	0.75	0.97
$\text{Hg} + \text{HCl} \rightarrow \text{HgCl} + \text{H}$	0.77	1.13	0.77	1.04
$\text{HgCl} + \text{HCl} \rightarrow \text{HgCl}_2 + \text{H}$	0.46	0.27	0.33	0.26
$\text{HgO} + \text{HCl} \rightarrow \text{M}$	0.04	0.06	0.05	0.06
$\text{M} \rightarrow \text{HgCl} + \text{OH}$	0.45	0.63	0.47	0.59
$\text{Hg} + \text{HgCl}_2 \rightarrow \text{Hg}_2\text{Cl}_2$ (Hg1)	0.92	0.89	0.92	0.86
$\text{Hg} + \text{HgCl}_2 \rightarrow \text{Hg}_2\text{Cl}_2$ (Hg2)	0.00	-0.14	0.00	-0.10
DIRAC-B3LYP	$1000\ln\beta_{202-198}^{\text{NV}}$			
$\text{Hg} + \text{HOCl} \rightarrow \text{HgCl} + \text{OH}$	0.69	0.97	0.70	0.97
$\text{Hg} + \text{HCl} \rightarrow \text{HgCl} + \text{H}$	0.72	1.04	0.72	1.03
$\text{HgCl} + \text{HCl} \rightarrow \text{HgCl}_2 + \text{H}$	0.43	0.25	0.31	0.26
$\text{HgO} + \text{HCl} \rightarrow \text{M}$	0.04	0.06	0.04	0.06
$\text{M} \rightarrow \text{HgCl} + \text{OH}$	0.42	0.58	0.43	0.59
$\text{Hg} + \text{HgCl}_2 \rightarrow \text{Hg}_2\text{Cl}_2$ (Hg1)	0.86	0.82	0.86	0.86
$\text{Hg} + \text{HgCl}_2 \rightarrow \text{Hg}_2\text{Cl}_2$ (Hg2)	0.00	-0.13	0.00	-0.10

better precision and accuracy. Generally, better correlations are observed for these equilibrium data (Figs. 1, 2, 3, 4). However, significant deviations of Reaction 5 are detected for these results calculated at the DHF level (Table 5). Such phenomenon indicates that such scaling methods for two types of electron densities at the nucleus, namely, the contact density $|\Psi(0)|^2$ and effective density $\bar{\rho}_e^A$, have different sensitivities to which type of NVE-induced isotope fractionation we are interested in. For these equilibrium NVEs, the different methods (DHF or B3LYP) used to describe electronic structure have limited

effects on the quality and errors of the fitting results. In other words, electron correlations seem to have negligible effects on the $\bar{\rho}_e^A$ of common Hg-incorporated molecules in the ground state. However, things are more complicated for these kinetic NVEs. A better linear correlation can be obtained when using the B3LYP method rather than the DHF. It indicates that for these systems with more complex electronic structures, i.e., transition states, more accurate descriptions of their electronic structures are necessary to guarantee the accuracy of the scaling method to estimate kinetic NVEs. Therefore, we recommend using

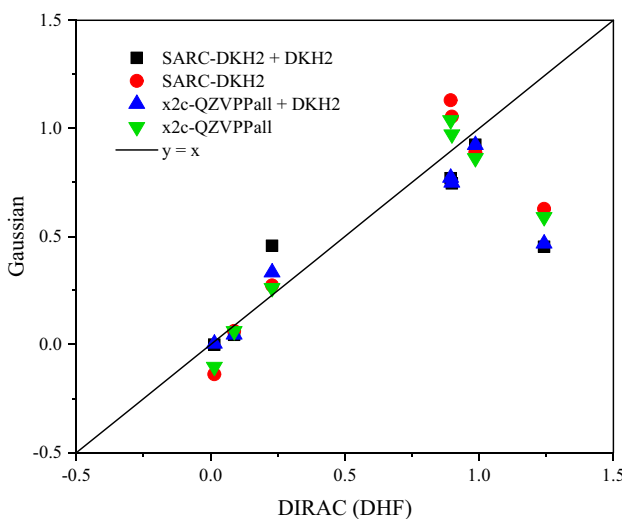


Fig. 5 The correlation between the kinetic Hg isotope fractionations ($1000\ln\beta_{202-198}$) (%) of Hg-related chloride species mercury oxide at 273.15 K calculated using the scaled contact densities from Gaussian09 and the effective densities from DIRAC19 (at the DHF level) with 4 different settings: SARC-DKH2; SARC-DKH2 + DKH2; x2c-QZVPPall; x2c-QZVPPall + DKH2

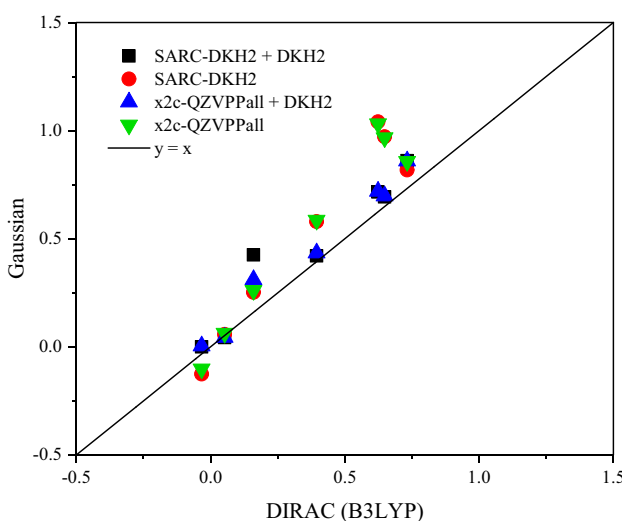


Fig. 6 The correlation between the kinetic Hg isotope fractionations ($1000\ln\beta_{202-198}$) (%) of Hg-related chloride species mercury oxide at 273.15 K calculated using the scaled contact densities from Gaussian09 and effective densities from DIRAC19 (at the B3LYP level) with 4 different settings: SARC-DKH2; SARC-DKH2 + DKH2; x2c-QZVPPall; x2c-QZVPPall + DKH2

more accurate methods such as DFT rather than DHF when calculating NVEs with $\bar{\rho}_e^A$ when using the DIRAC package.

Finally, we chose to use these results calculated at the B3LYP level with DIRAC19 for all 6 subsequent reactions. For these results obtained by $\Delta|\Psi(0)|_s^2$, the fitting results in Fig. 3 show a maximum deviation of $\pm 0.15\%$ for

$1000\ln\beta_{202-198}^{\text{NV}}$ at 273.15 K, which can be directly used as a scale for systematic errors of the scaling method we used in this study.

4.2 NVE-induced kinetic Hg isotope fractionation during mercury oxidation by chlorine species

Taking $^{202}\text{Hg}/^{198}\text{Hg}$ at 273.15 K as an example, all the $1000\ln\beta_{202-198}^{\text{MD}}$, $1000\ln\beta_{202-198}^{\text{NV}}$ and total fractionations $1000\ln\beta_{202-198}$ at 273.15, 298.15, 373.15, 573.15 and 1273.15 K calculated at the B3LYP level with DIRAC19 for Reactions 1, 2, 3, 4, 5, 6 are summarized in Table 6. For MDFs at 273.15 K, Reactions 1, 2, 3 show abnormal KIEs of $+0.13\%$, $+0.25\%$ and $+0.63\%$, respectively, indicating that heavy ^{202}Hg reacts faster than light ^{198}Hg . Reactions 4, 5, 6 show normal KIEs of -1.74% , -1.23% and $(-1.11\% \text{ for Hg1 atom and } -2.28\% \text{ for Hg2 atom})$, where ^{198}Hg reacts faster than ^{202}Hg . Things are simpler for NVE-induced MIFs at 273.15 K, all 6 reactions show abnormal KIEs from 0.00% (Hg2 atom of Reaction 6) to $+0.86\%$ (Hg1 atom of Reaction 6). For total KIEs at 273.15 K, Reactions 1, 2, 3 show an abnormal KIE of $+0.83\%$, $+0.96\%$ and $+0.94\%$, respectively, in which Reactions 1 and 2 are mainly caused by the relatively large abnormal NVE of $+0.70\%$ and $+0.72\%$, and Reaction 3 mainly is caused by the relatively large abnormal MDF of $+0.63\%$.

Additionally, we noticed that the KIEs for Reaction 1 will even be reversed if the NVEs are not included at 573.15 K and 1273.15 K, i.e., -0.09% to $+0.24\%$ and -0.14% to 0.01% , respectively. Therefore, we believe that the NVE plays an important role on accurate estimations of KIEs for Hg isotopes. Meanwhile, similar inferences can be reached for other heavy isotope systems with significant NVEs, such as Pb, Tl, and U.

4.3 KIEs of Hg isotopes and their geochemical implications

Hg isotopes have been widely used to trace multiple processes through different patterns in the geochemistry and environmental sciences communities: $\Delta^{199}\text{Hg}$ vs. $\delta^{202}\text{Hg}$, $\Delta^{200}\text{Hg}$ vs. $\delta^{202}\text{Hg}$, $\Delta^{204}\text{Hg}$ vs. $\delta^{202}\text{Hg}$ and $\Delta^{199}\text{Hg}$ vs. $\Delta^{201}\text{Hg}$ (e.g., Blum et al. 2014). Figures 7, 8, 9, 10 show the relationships between $\Delta^{199}\text{Hg}$ and $\delta^{202}\text{Hg}$ (odd MIF and MDF), $\Delta^{200}\text{Hg}$ and $\delta^{202}\text{Hg}$ (even MIF and MDF), $\Delta^{204}\text{Hg}$ and $\delta^{202}\text{Hg}$ (even MIF and MDF) and $\Delta^{199}\text{Hg}$ and $\Delta^{201}\text{Hg}$, respectively. The data points in Fig. 7 fall on a line with a slope of -0.008 , and Reactions 1, 2, 3 show a trend consistent with that of fractionation during microbial reduction of Hg(II) and demethylation of MeHg. Reactions 4, 5, 6 are similar to the behavior of the methylation of mercury (II) by sulfate-reducing bacteria. The

Table 5 Standard deviation and mean absolute deviation between the scaled contact density and effective density

DIRAC method	DHF		B3LYP	
	Reactions	Standard deviation	Mean absolute deviation	Standard deviation
$\text{Hg} + \text{HOCl} \rightarrow \text{HgCl} + \text{OH}$	10.0	9.7	13.7	10.0
$\text{Hg} + \text{HCl} \rightarrow \text{HgCl} + \text{H}$	11.9	11.4	18.6	14.5
$\text{HgCl} + \text{HCl} \rightarrow \text{HgCl}_2 + \text{H}$	9.4	7.5	11.3	10.1
$\text{HgO} + \text{HCl} \rightarrow \text{M}$	2.6	2.5	0.8	0.6
$\text{M} \rightarrow \text{HgCl} + \text{OH}$	52.0	51.7	7.9	5.8
$\text{Hg} + \text{HgCl}_2 \rightarrow \text{Hg}_2\text{Cl}_2 (\text{Hg 1})$	6.6	6.4	4.0	3.8
$\text{Hg} + \text{HgCl}_2 \rightarrow \text{Hg}_2\text{Cl}_2 (\text{Hg2})$	7.0	5.3	4.5	4.2

Table 6 Calculated KIE fractionation factors for the kinetics of mercury oxidation by chlorine species (‰), including conventional mass-dependent ($1000\ln\beta_{202-198}^{\text{MD}}$), nuclear volume effect ($1000\ln\beta_{202-198}^{\text{NV}}$) and total ($1000\ln\beta_{202-198}$) fractionation factors

Reaction	273.15 K	298.15 K	373.15 K	573.15 K	1273.15 K
MD fractionation ($1000\ln\beta_{202-198}^{\text{MD}}$)					
$\text{Hg} + \text{HOCl} \rightarrow \text{HgCl} + \text{OH}$	0.13	0.09	0.00	-0.09	-0.14
$\text{Hg} + \text{HCl} \rightarrow \text{HgCl} + \text{H}$	0.25	0.21	0.13	0.06	0.01
$\text{HgCl} + \text{HCl} \rightarrow \text{HgCl}_2 + \text{H}$	0.63	0.53	0.34	0.14	0.01
$\text{HgO} + \text{HCl} \rightarrow \text{M}$	-1.74	-1.65	-1.48	-1.27	-1.14
$\text{M} \rightarrow \text{HgCl} + \text{OH}$	-1.23	-1.23	-1.24	-1.24	-1.24
$\text{Hg} + \text{HgCl}_2 \rightarrow \text{Hg}_2\text{Cl}_2 (\text{Hg1})$	-1.11	-1.17	-1.27	-1.38	-1.44
$\text{Hg} + \text{HgCl}_2 \rightarrow \text{Hg}_2\text{Cl}_2 (\text{Hg2})$	-2.28	-2.23	-2.13	-2.02	-1.95
NVE fractionation ($1000\ln\beta_{202-198}^{\text{NV}}$)					
$\text{Hg} + \text{HOCl} \rightarrow \text{HgCl} + \text{OH}$	0.70	0.64	0.51	0.33	0.15
$\text{Hg} + \text{HCl} \rightarrow \text{HgCl} + \text{H}$	0.72	0.66	0.53	0.34	0.15
$\text{HgCl} + \text{HCl} \rightarrow \text{HgCl}_2 + \text{H}$	0.31	0.28	0.23	0.15	0.07
$\text{HgO} + \text{HCl} \rightarrow \text{M}$	0.04	0.04	0.03	0.02	0.01
$\text{M} \rightarrow \text{HgCl} + \text{OH}$	0.43	0.40	0.32	0.21	0.09
$\text{Hg} + \text{HgCl}_2 \rightarrow \text{Hg}_2\text{Cl}_2 (\text{Hg1})$	0.86	0.79	0.63	0.41	0.18
$\text{Hg} + \text{HgCl}_2 \rightarrow \text{Hg}_2\text{Cl}_2 (\text{Hg2})$	0.00	0.00	0.00	0.00	0.00
Total fractionation ($1000\ln\beta_{202-198}$)					
$\text{Hg} + \text{HOCl} \rightarrow \text{HgCl} + \text{OH}$	0.83	0.72	0.51	0.24	0.01
$\text{Hg} + \text{HCl} \rightarrow \text{HgCl} + \text{H}$	0.96	0.86	0.66	0.40	0.17
$\text{HgCl} + \text{HCl} \rightarrow \text{HgCl}_2 + \text{H}$	0.94	0.82	0.57	0.28	0.08
$\text{HgO} + \text{HCl} \rightarrow \text{M}$	-1.69	-1.61	-1.44	-1.25	-1.13
$\text{M} \rightarrow \text{HgCl} + \text{OH}$	-0.80	-0.84	-0.92	-1.03	-1.15
$\text{Hg} + \text{HgCl}_2 \rightarrow \text{Hg}_2\text{Cl}_2 (\text{Hg1})$	-0.25	-0.38	-0.64	-0.97	-1.25
$\text{Hg} + \text{HgCl}_2 \rightarrow \text{Hg}_2\text{Cl}_2 (\text{Hg2})$	-2.27	-2.22	-2.12	-2.02	-1.95

data points fall on lines with slopes of 0.001 in Fig. 8, in which no significant even-numbered Hg isotope anomalies were found. The data points fall on lines with slopes of 0.026 in Fig. 9, and there is a negative even-numbered Hg isotope anomaly (Reaction 5). A small amount of odd-MIF (<~0.5‰) can be produced in equilibrium and kinetic reactions due to the nuclear volume effect (Blum and Johnson 2017). We speculate the negative anomaly is also caused by nuclear volume effect. The slope in Fig. 10 is 1.589, which is larger than the boundary range of 1.00

and 1.36 for natural samples measured by Blum et al. (2014). This is consistent with the current thought that the value of $\Delta^{199}\text{Hg}$ vs. $\Delta^{201}\text{Hg}$ produced by NVE is about 1.6 (Ghosh et al. 2013). As mercury is a highly redox sensitive element and the only metal element in nature with mass fractionation (MDF) and non-mass fractionation (MIF), the isotopic composition of mercury varies in different degrees in chemical reactions such as atmosphere, ocean and sediments (Blum and Johnson 2017; Sherman et al. 2010). Therefore, MDF and MIF of mercury isotopes

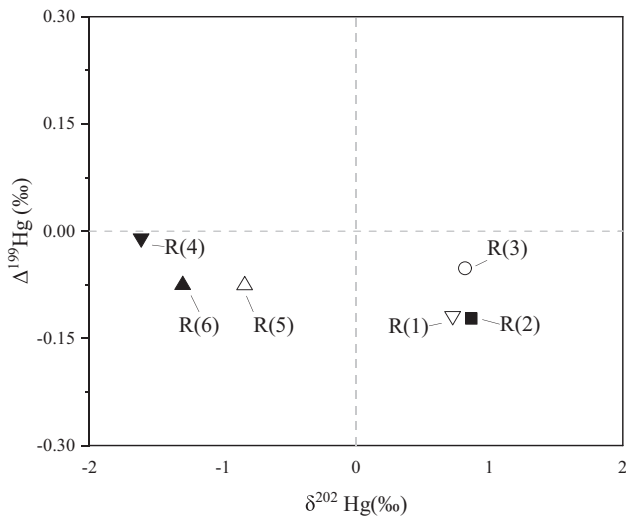


Fig. 7 Plot of $\Delta^{199}\text{Hg}$ versus $\delta^{202}\text{Hg}$ for Reactions 1, 2, 3, 4, 5, 6 at different temperatures. The hollow inverted triangle represents Reaction (1), the filled square represents Reaction (2), the hollow circle represents Reaction (3), the solid inverted triangle represents Reaction (4), the hollow triangle represents Reaction (5), and the filled triangle represents Reaction (6)

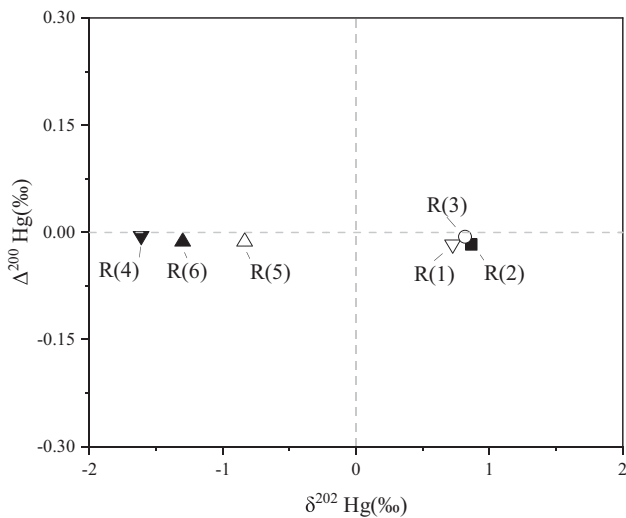


Fig. 8 Plot of $\Delta^{200}\text{Hg}$ versus $\delta^{202}\text{Hg}$ for Reactions 1, 2, 3, 4, 5, 6 at different temperatures. The hollow inverted triangle represents Reaction (1), the filled square represents Reaction (2), the hollow circle represents Reaction (3), the solid inverted triangle represents Reaction (4), the hollow triangle represents Reaction (5), and the filled triangle represents Reaction (6)

can accurately trace the biogeochemical processes of the Earth's surface and mercury pollution, reveal the evolution of planets, identify large igneous provinces in geological history, and trace the sources of mineral deposits (Xu et al.

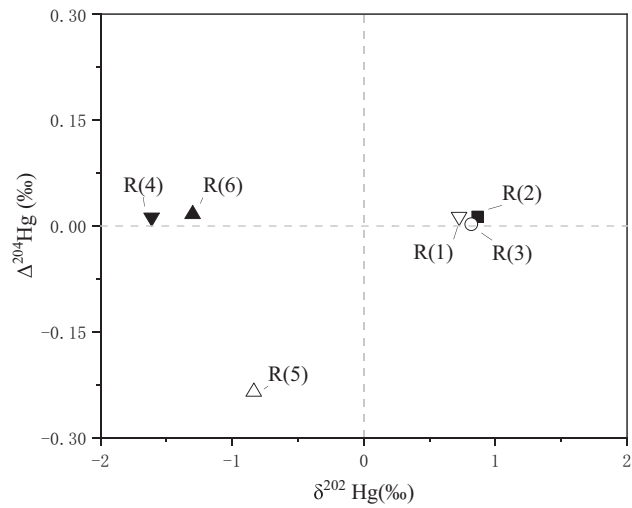


Fig. 9 Plot of $\Delta^{204}\text{Hg}$ versus $\delta^{202}\text{Hg}$ for Reactions 1, 2, 3, 4, 5, 6 at different temperatures. The hollow inverted triangle represents reaction (1), the filled square represents reaction (2), the hollow circle represents reaction (3), the solid inverted triangle represents reaction (4), the hollow triangle represents reaction (5), and the filled triangle represents reaction (6)

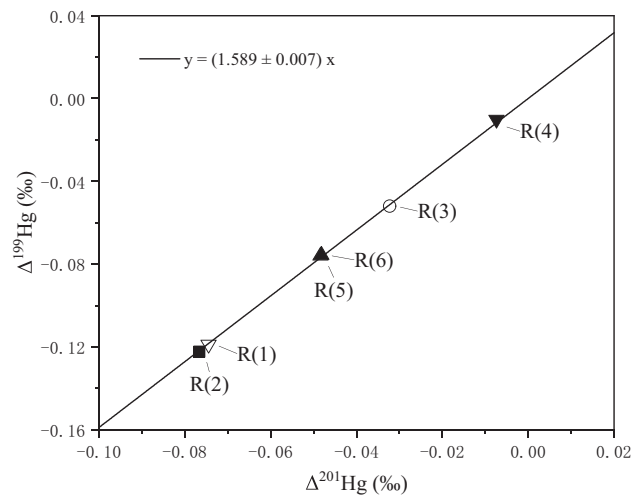


Fig. 10 Plot of $\Delta_{\text{NV}}^{199}\text{Hg}$ versus $\Delta_{\text{NV}}^{201}\text{Hg}$ for Reactions 1, 2, 3, 4, 5, 6 using x2c-QZVPPall+DKH2 and DIRAC-B3LYP at different temperatures. The hollow inverted triangle represents Reaction (1), the filled square represents Reaction (2), the hollow circle represents Reaction (3), the solid inverted triangle represents Reaction (4), the hollow triangle represents Reaction (5), and the filled triangle represents Reaction (6)

2021). The study on the fractionation mechanism of mercury isotopes and the genesis of ore deposits requires more verification of abnormal fractionation such as $\Delta^{202}\text{Hg}$ and $\Delta^{204}\text{Hg}$ (Blum and Johnson 2017).

5 Conclusion

In this paper, the equilibrium mass dependence and nuclear volume fractionations of mercury-related substances (Hg^0 , Hg^+ , Hg^{2+} , HgCl_2 , HgBr_2 , $\text{Hg}(\text{CH}_3)_2$, $\text{Hg}(\text{CH}_3)\text{Cl}$, $[\text{Hg}(\text{H}_2\text{O})_6]^{2+}$, $\text{Hg}(\text{OH})_2$ and $[\text{HgCl}_4]^{2-}$) are calculated with both energy and electron density methods. Additionally, the accuracy and errors for the method of scaling contact density to reproduce correct effective density for calculating NVEs are evaluated. Finally, 6 Hg oxidation reactions through chlorine-related species are chosen to estimate the KIEs of the MDFs and NVE-induced MIFs. The following conclusions can be obtained: 1. NVEs calculated through effective density show excellent agreements with those data calculated by taking electronic energy differences from Schäuble (2007) and Yang and Liu (2015, 2016). 2. These scaled contact densities calculated with the x2c-QZVPPall basis set considering the DKH2 relativistic correction at the B3LYP level using Gaussian09 D.01 and Multiwfn 3.8(dev) can be good candidates reproducing more precise and accurate effective density data by DIRAC19 at the same B3LYP level with four-component relativistic Hamiltonians for NVE calculations. 3. Taking $^{202}\text{Hg}/^{198}\text{Hg}$ as an example, significant NVE-induced KIEs for Reactions 1, 2, 3, 4, 5, 6 at 273.15 K are obtained from 0.00‰ to –0.80‰. 4. Taking NVEs into account, these KIEs of Hg oxidation by chlorin species can serve as new tracers for Hg isotope research with $\Delta^{199}\text{Hg}$ vs. $\delta^{202}\text{Hg}$, $\Delta^{200}\text{Hg}$ vs. $\delta^{202}\text{Hg}$ and $\Delta^{199}\text{Hg}$ vs. $\Delta^{201}\text{Hg}$.

Acknowledgements This paper is supported by Chinese NSF project (42130114), the strategic priority research program (B) of CAS (XDB41000000) and the pre-research Project on Civil Aerospace Technologies No. D020202 funded by Chinese National Space Administration (CNSA)

Author contribution Yining Zhang and Yun Liu selected topics; Yining Zhang conceived and designed methods; Chenlu Yang calculated data, analyzed and compiled the first draft; Yining Zhang and Yun Liu reviewed and revised the first draft.

Funding Chinese NSF project (42130114), the strategic priority research program (B) of CAS (XDB41000000) and the pre-research Project on Civil Aerospace Technologies (No. D020202) funded by Chinese National Space Administration (CNSA).

Data availability All data and models used during the study appear in the submitted article.

Code availability N/A.

Declarations

Conflict of interest The authors declare that they have no competing interests.

Ethical approval N/A.

Consent to participate N/A.

Consent for publication N/A.

References

- Almoukhalaati A, Shee A, Sae T (2016) Nuclear size effects in vibrational spectra. *Phys Chem Chem Phys*. 18:15406–15417.
- Angeli I (2004) A consistent set of nuclear rms charge radii: Properties of the radius surface R(N, Z). *Atom Data Nucl Data Tables*. 87:185–206.
- Angeli I, Marinova KP (2013) Table of experimental nuclear ground state charge radii: An update. *Atom Data Nucl Data Tables*. 99(1):69–95.
- Aufmuth P, Heilig K, Steudel A (1987) Changes in mean-square nuclear charge radii from optical isotope shifts. *Atom Data Nucl Data Tables*. 37:455–490.
- Barysz M, Sadlej AJ (2001) Two-component methods of relativistic quantum chemistry: from the Douglas-Kroll approximation to the exact two-component formalism. *J Mol Struct*. 573:181–200.
- Becke AD (1993) Density-functional thermochemistry. III. The role of exact exchange. *J Chem Phys*. 98:5648–5652.
- Bergquist BA, Blum JD (2007) Mass-dependent and -independent fractionation of Hg isotopes by photoreduction in aquatic systems. *Science*. 318:417–420.
- Bergquist BA, Blum JD (2009) The odds and evens of mercury isotopes: Applications of mass-dependent and mass-independent isotope fractionation. *Elements*. 5(6):53–357.
- Bigeleisen J (1996) Nuclear size and shape effects in chemical reactions. Isotope chemistry of the heavy elements. *J Am Chem Soc*. 118:3676–3680.
- Bigeleisen J, Mayer MG (1947) Calculation of equilibrium constants for isotopic exchange reactions. *J Chem Phys*. 15:261–267.
- Bigeleisen J, Wolfsberg M (1958) Theoretical and experimental aspects of isotope effects in chemical kinetics. *Adv Chem Phys*. 1:15–76.
- Blum JD (2011) Applications of stable mercury isotopes to biogeochemistry. *Handbook of environmental isotope geochemistry*, Vol 15. Springer, Cham, pp 229–245.
- Blum JD, Johnson MW (2017) Recent developments in mercury stable isotope analysis. *Rev Min Geochem*. 82(1):733–757.
- Blum JD, Sherman LS, Johnson MW (2014) Mercury isotopes in Earth and environmental sciences. *Ann Rev Earth Planet Sci*. 42(1):249–269.
- Chen JB, Hintelmann H, Feng XB, Dimock B (2012) Unusual fractionation of both odd and even mercury isotopes in precipitation from Peterborough, ON, Canada. *Geochim Cosmochim Acta*. 90:33–46.
- Dunning TH (1989) Gaussian basis sets for use in correlated molecular calculations. I. The atoms boron through neon and hydrogen. *J Chem Phys*. 90:1007–1023.
- KGDyall2023Dyall double-zeta, triple-zeta, and quadruple-zeta basis set archive filesZenodo10.5281/zenodo.7606547Dyall KG (2023) Dyall double-zeta, triple-zeta, and quadruple-zeta basis set archive files. Zenodo. <https://doi.org/10.5281/zenodo.7606547>
- Dzurko M, Foucher D, Hintelmann H (2009) Determination of compound-specific Hg isotope ratios from transient signals using gas chromatography coupled to multicollector inductively coupled plasma mass spectrometry (MC-ICP/MS). *Anal Bioanal Chem*. 393(1):345–355.
- Estrade N, Carignan J, Sonke JE, Donard OFX (2009) Mercury isotope fractionation during liquid–vapor evaporation experiments. *Geochim Cosmochim Acta*. 73:2693–2711.
- Eyring H (1935) The activated complex in chemical reactions. *J Chem Phys*. 3:107–115.
- Fang T, Liu Y (2019) Equilibrium thallium isotope fractionation and its constraint on Earth's late veneer. *Acta Geochim*. 38(4):459–471.

- Franzke YJ, Spiske L, Pollak P, Weigend F (2020) Segmented contracted error-consistent basis sets of quadruple- ζ valence quality for one- and two-component relativistic all-electron calculations. *J Chem Theory Comput.* 16:5658–5674.
- Fricke G, Heilig K (2004) 80-Hg mercury. Numerical data and functional relationships in science and technology. Group I: Element particles, nuclei and atoms. Nuclear charge radii, Vol 20. Springer, Heidelberg, pp 1–9.
- Frisch MJ et al (2009) Gaussian software package, Gaussian09, Revision D.01. Inc, Wallingford CT.
- Fu SL, Hu RZ, Yin RS, Yan J, Mi XF, Song ZC, Sullivan NA (2020) Mercury and *in-situ* sulfur isotopes as constraints on the metal and sulfur sources for the world's largest Sb deposit at Xikuangshan, southern China. *Min Depos.* 55:1353–1364.
- Fujii T, Moynier F, Albarède F (2009) The nuclear field shift effect in chemical exchange reactions. *Chem Geol.* 267:139–156.
- Ghosh S, Schauble EA, Couloume GL, Blum JD, Bergquist BA (2013) Estimation of nuclear volume dependent fractionation of mercury isotopes in equilibrium liquid-vapor evaporation experiments. *Chem Geol.* 336:5–12.
- Gomes ASP et al (2019) DIRAC a relativistic ab initio electronic structure program, Release DIRAC19. <https://doi.org/10.5281/zenodo.3572669>
- Grimme S (2006) Semiempirical hybrid density functional with perturbative second-order correlation. *J Chem Phys.* 124:1–16.
- Grimme S, Antony J, Ehrlich S, Krieg H (2010) A consistent and accurate ab initio parameterization of density functional dispersion correction (DFT-D) for the 94 elements H–Pu. *J Chem Phys.* 132:1–19.
- King WH (1984) Isotope shifts in atomic spectra. Plenum Press, New York.
- Li LC, Deng P, Tian AM, Xu MH, Zheng CG, Wong NB (2003) A study on the reaction mechanism and kinetic of mercury oxidation by chlorine species. *J Mol Struct. (Theochem)* 625:277–281.
- Li ZG, Feng XB, He TR, Yan HY, Liang L (2005) Determination of total mercury in soil and sediment by aqua regia digestion in the water bath coupled with cold vapor atom fluorescence spectrometry. *Bull Min Pet Geochem.* 24(2):140–143.
- Li SL, Li LH, Lan YC, Lv BY (2016) Rapid determination of total mercury in sediment by using Lumex analytical equipment. *Guangzhou Chem.* 41(2):68–71.
- Lin HL, Zhu RL, Yu L, Cheng YX, Zhu RR, Liu P, Ren ZH (2020) Determination of arsenic, mercury, selenium, antimony and bismuth in soil and sediments by water bath digestion–atomic fluorescence spectrometry. *Spectrosc Spectr Anal.* 40(5):1528–1533.
- Liu YF, Qi HW, Bi XW, Hu RZ, Qi LK, Yin RS, Tang YY (2021) Mercury and sulfur isotopic composition of sulfides from sediment-hosted lead–zinc deposits in Lanping basin Southwestern China. *Chem Geol.* 559:119910.
- Lu T, Chen F (2012) Multiwfns: A multifunctional wavefunction analyzer. *J Comput Chem.* 33:580–592.
- Pantazis DA, Chen XY, Landis CR, Neese F (2008) All-electron scalar relativistic basis sets for third-row transition metal atoms. *J Chem Theory Comput.* 4(6):908–919.
- Peterson KA, Puzzarini C (2005) Systematically convergent basis sets for transition metals. II. Pseudopotential-based correlation consistent basis sets for the group 11 (Cu, Ag, Au) and 12 (Zn, Cd, Hg) elements. *Theor Chem Acc.* 114:283–296.
- Redlich O (1935) Eine allgemeine beziehung zwischen den schwingungsfrequenzen isotoper molekülen. *Z Phys Chem B.* 28:371–382 (in German).
- Schauble EA (2007) Role of nuclear volume in driving equilibrium stable isotope fractionation of mercury, thallium, and other very heavy elements. *Geochim Cosmochim Acta.* 71:2170–2189.
- Schauble EA (2013) Modeling nuclear volume isotope effects in crystals. *Proc Natl Acad Sci USA.* 110:17714–17719.
- Sherman LS, Blum JD, Johnson KP, Keeler GJ, Barres JA, Douglas TA (2010) Mass-independent fractionation of mercury isotopes in arctic snow driven by sunlight. *Nat Geosci.* 3:173–177.
- Sial AN, Lacerda LD, Ferreira VP, Frei R, Marquillas RA, Barbosa JA, Gaucher C, Windmöller CC, Pereira NS (2013) Mercury as a proxy for volcanic activity during extreme environmental turnover: The Cretaceous–Paleogene transition. *Palaeogeogr Palaeoclimatol Palaeoecol.* 387(7):153–164.
- Smith CN, Kesler SE, Klaue B, Blum JD (2005) Mercury isotope fractionation in fossil hydrothermal systems. *Geology.* 33(10):825–828.
- Stacey DN (1966) Isotope shifts and nuclear charge distributions. *Rep Prog Phys.* 29:171–215.
- Sun RY, Sonke JE, Liu GJ (2016) Biogeochemical controls on mercury stable isotope compositions of world coal deposits: A review. *Earth Sci Rev.* 152:1–13.
- Sun T, Gaut A, Tang S, Huang YX, ElSherief M, Zhao JY, Mirza D, Belding E, Chang KW, Wang WY (2019) Mitigating gender bias in natural language processing: Literature review. *Comput Linguist Assoc.* 57:1630–1640.
- Thibodeau AM, Ritterbush K, Yager JA, Joshua West A, Ibarra Y, Bottjer DJ, Berelson WM, Bergquist BA, Corsetti FA (2016) Mercury anomalies and the timing of biotic recovery following the end-Triassic mass extinction. *Nat Commun.* 7:1–8.
- Urey HC (1947) The thermodynamic properties of isotopic substances. *J Chem Soc.* <https://doi.org/10.1039/jr9470000562>
- Weigend F, Ahlrichs R (2005) Balanced basis sets of split valence, triple zeta valence and quadruple zeta valence quality for H to Rn: Design and assessment of accuracy. *Phys Chem Chem Phys.* 7(18):3297–3305.
- Wilson AK, Woon DE, Peterson KA, Dunning TH Jr (1999) Gaussian basis sets for use in correlated molecular calculations. IX. the atoms gallium through krypton. *J Chem Phys.* 110:7667–7676.
- Xu CX, Yin RS, Peng JT, Hurley JP, Lepak RF, Gao JF, Feng XB, Hu RZ, Bi XW (2018) Mercury isotope constraints on the source for sediment-hosted lead–zinc deposits in the Changdu Area, southwestern China. *Miner Deposita.* 53:339–352.
- Xu CX, Meng YM, Huang C, Tang C, Zheng FW (2021) Advances in the study on mercury isotope geochemistry and its application in mineral deposits. *Rock Miner Anal.* 40(2):173–186.
- Yang S, Liu Y (2015) Nuclear volume effects in equilibrium stable isotope fractionations of mercury, thallium and lead. *Sci Rep.* 5:1–10.
- Yang S, Liu Y (2016) Nuclear field shift effects on stable isotope fractionation: A review. *Acta Geochim.* 35(3):227–239.
- Yin RS, Feng XB, Chen J (2014) Mercury stable isotopic compositions in coals from major coal producing fields in China and their geochemical and environmental implications. *Environ Sci Technol.* 48(10):5565–5574.
- Zhu CW, Tao CH, Yin RS, Liao SL, Yang WF, Liu J, Barriga FJAS (2020) Seawater versus mantle sources of mercury in sulfide-rich seafloor hydrothermal systems, southwest Indian Ridge. *Geochim Cosmochim Acta.* 281:91–101.

Springer Nature or its licensor (e.g. a society or other partner) holds exclusive rights to this article under a publishing agreement with the author(s) or other rightsholder(s); author self-archiving of the accepted manuscript version of this article is solely governed by the terms of such publishing agreement and applicable law.